

Inland-LOAM: Voxel-Based Structural Semantic LiDAR Odometry and Mapping for Inland Waterway Navigation

Zhongbi Luo, Yunjia Wang, Jan Swevers, Peter Slaets and Herman Bruyninckx

Abstract—Accurate and up-to-date geospatial information is crucial for enhancing the safety and autonomy of Inland Waterway Transport (IWT). Existing Inland Electronic Navigational Charts (IENCs) often lack real-time detail, and conventional LiDAR-based Simultaneous Localization and Mapping (SLAM) methods struggle with waterway characteristics like unstructured geometric features and water surface reflections. These challenges lead to significant localization drift and produce point cloud maps lacking the semantic richness required for autonomous decision-making. This paper introduces a comprehensive LiDAR odometry and Mapping framework for inland waterway navigation (Inland-LOAM). We present an improved feature extraction method adapted to unique waterway geometries, combined with a joint optimization that incorporates the water surface as a global planar constraint to mitigate drift. We also propose an innovative pipeline that transforms dense 3D point cloud outputs into structured 2D semantic maps. By constructing semantic voxel grids and performing geometric analyses (roughness, planarity, and slope), our system classifies the environment into meaningful structural categories and supports real-time computation of critical parameters like vertical bridge clearances. An automated module then efficiently extracts shoreline boundaries, exporting them into a lightweight, IENC-compatible format. Extensive evaluations on a diverse, real-world dataset demonstrate that Inland-LOAM achieves superior localization accuracy over state-of-the-art methods. The generated maps and shorelines align with real-world conditions, providing reliable information to enhance navigational situational awareness. Both the dataset and the algorithm are publicly available to support future research.

Index Terms—LiDAR SLAM, semantic mapping, Sensor technology, Computer vision, Maritime transportation, Connected and Autonomous Vehicles.

I. INTRODUCTION

IWT constitutes an essential component of Europe's freight infrastructure, spanning a network exceeding 41,000 km, interlinking major cities and industrial hubs across 13 interconnected Member States [1]. As efforts increase to shift freight from congested road and rail networks, the importance of accurate geospatial information and detailed environmental models for managing and navigating these waterways grows [2]. However, navigating these waterways involves safety risks,

with studies identifying human error as the primary cause in up to 70% of maritime incidents [3]. In this context, advancements in automation, especially the deployment of uncrewed surface vehicles (USVs), are driving a transformation in inland waterway transport. USVs play a crucial role not only by mitigating the risks associated with human factors, but also by promising improved cargo transport efficiency and facilitating innovative logistics services, including operations within challenging environments such as congested urban canal networks [4]. However, the effective operation of USVs is challenging due to the complex and dynamic nature of inland waterways. These are confined channels with locks and (movable and fixed) bridges and limited draft, which often create navigation bottlenecks [5]. Safe and efficient navigation mainly depends on robust systems for perception, localization, and mapping. These systems must enable the vessel to reliably recognize diverse surroundings, including shorelines, infrastructure, vegetation, and overhead obstacles such as bridges, to operate safely.

Traditionally, navigation on inland waterways relies highly on Global Navigation Satellite Systems (GNSS) for positioning, complemented by standard nautical charts like IENC for contextual spatial data [6]. However, GNSS frequently suffers from severe attenuation or complete outages in typical IWT scenarios, particularly during passages under bridges, within narrow urban canals flanked by tall buildings "urban canyons", or along waterways with dense vegetation canopies [7], [8]. This documented unreliability highlights the need for onboard localization systems that work independently [9]. Furthermore, existing geospatial data products, IENC, while providing important routing and regulatory data, often lack the spatial detail or real-time updates required for accurate autonomous maneuvering and perception. Representations of shorelines and their surrounding features, including vegetation, shoreline constructions, and other obstacles, are often generalized or outdated in existing maps [10], [11]. A key limitation of IENC is the representation of safety parameters, such as vertical bridge clearance, using static data. This approach fails to account for dynamic water level variations, a significant operational challenge in IWT affecting actual clearances [12]. As a result, relying on static, low-resolution geospatial information hinders the deployment of advanced autonomous functions.

LiDAR-based SLAM has developed as a strong technique in terrestrial robotics and autonomous driving, making it possible to build precise 3D maps and accurate localization even in environments without GNSS [13], [14]. Applying LiDAR SLAM to the IWT is a viable way to overcome the limitations of previous approaches. However, traditional

Corresponding author: Zhongbi Luo.

Zhongbi Luo, Peter Slaets, Jan Swevers and Herman Bruyninckx are with the Division of Robotics, Automation and Mechatronics in the Department of Mechanical Engineering, KU Leuven, 3001 Leuven, Belgium (e-mail: zhongbi.luo@kuleuven.be; peter.slaets@kuleuven.be; jan.swevers@kuleuven.be; herman.bruyninckx@kuleuven.be)

Yunjia Wang is with the Division of Declarative Languages and Artificial Intelligence (DTAI) in the Department of Computer Science, KU Leuven, 8200 Bruges, Belgium (e-mail: yunjia.wang@kuleuven.be).

Yunjia Wang, Jan Swevers and Herman Bruyninckx are also with Flanders Make@KU Leuven, 3001 Leuven, Belgium. Herman Bruyninckx is also with the Department of Mechanical Engineering, the TU Eindhoven, 5612 AZ Eindhoven, The Netherlands.



Fig. 1: Our experimental platform, a catamaran named the Maverick, was equipped with a Sensor Box for situational awareness and data collection. Image source: [17].

LiDAR SLAM algorithms face particular challenges in this context. The main challenges come from the structure of the environment: unlike urban scenes with abundant planar facades (buildings) and consistent features (lane markings), inland waterways predominantly feature irregular, natural shorelines often covered with vegetation [12]. This lack of structured geometry and standardized visual cues affects the reliable extraction of edges and planar features necessary by algorithms like LOAM [15] and LeGO-LOAM [16]. Although this lack of structured geometry presents a challenge, these environments simultaneously offer a unique and powerful geometric prior that is often absent in terrestrial scenarios: the water surface itself. Rather than being treated as a source of interference, we contend that when properly detected, the inland water surface provides a vast, naturally occurring, and globally referenced planar constraint. This offers a simple, yet robust anchor to mitigate drift, particularly for roll, pitch, and altitude - a benefit not available from the smaller, localized planes found in typical indoor or urban environments. In addition to these algorithmic challenges, the development and evaluation of SLAM algorithms for IWT is hindered by the lack of suitable benchmark datasets.

Beyond achieving accurate geometric reconstruction, effective environmental understanding demands semantic understanding, e.g., distinguishing navigable water from vegetated banks, identifying a potential docking quay wall, or determining safe passage under a bridge. Standard SLAM methods typically do not provide this layer of structural semantic information. Finally, a gap exists in translating the rich, high-resolution data from SLAM systems into formats aligned with IENC navigation standards.

To address these challenges, we propose Inland-LOAM, a novel voxel-based system designed for structural semantic mapping in inland waterway environments. This method achieves robust LiDAR-based localization and mapping adapted for water surfaces, extracts structural semantic information using geometric analysis within a voxel map, and generates enhanced environmental representations suitable for navigation and integration with standard chart formats. The contributions of this paper are as follows:

- 1) Inland-LOAM is specifically enhanced for robustness in GNSS-denied inland waterway environments through improved feature extraction performance and the incorporation of water surface optimization to mitigate the prevalent vertical drift in inland waterway navigation.
- 2) A novel voxel-based structural semantic mapping approach using roughness, planarity, and slope analysis to generate 2D maps and calculating real-time bridge clearance.
- 3) An automated map conversion method to translate the high-detail structural semantic SLAM map into an IENC-compatible.
- 4) The proposed framework was demonstrated in a diverse set of real-world inland waterway scenes, including ports, urban canals, vegetated banks, bridges, and lifting gates. The experimental platform used for data collection is shown in Figure 1. All data are released as part of the publicly available dataset to support further research.

II. RELATED WORK

This section reviews existing literature relevant to LiDAR-based mapping and semantic understanding in the context of inland waterways, focusing on inland mapping methodologies, LiDAR odometry techniques, semantic scene understanding, and map integration with navigation standards.

A. Mapping in Inland Waterway Environments

LiDAR-based onboard mapping offers a promising solution for detailed mapping in inland scenarios [18], [19], [20], [21]. However, deploying LiDAR SLAM in IWT presents distinct complexities compared to established terrestrial applications [22], [23]:

Water surface Interference: Reflections on the surface can distort LiDAR returns, causing noisy or inaccurate measurements. Also, signal absorption along the z-axis weakens vertical constraints [24]. Due to continuous motion induced by waves and currents, vessels cannot be modeled using non-holonomic motion constraints [25].

Long Trajectories and Sparse Loops: The nature of waterway transport involves long traverses with infrequent returns to previously mapped areas, demanding high odometry accuracy due to limited opportunities for loop closure [26].

Data Scarcity: The robust evaluation of SLAM algorithms is hampered by the lack of comprehensive public data sets that capture the various conditions (narrow canals, locks, vegetation, bridges) and operational realities of European IWT; existing datasets like USVInland [27] often have limitations in scope or relevance.

B. LiDAR Odometry and Mapping and Variants

LOAM [15] pioneered efficient, real-time LiDAR odometry based on the roughness of each point on its respective ring. Its low drift and computational efficiency placed it among the top-3 methods on the KITTI odometry benchmark [28]. LeGO-LOAM [16] built upon LOAM by incorporating point cloud segmentation to separate ground points from other

objects and clustering non-ground points. This allows focusing feature extraction on more salient objects and significantly reduces computational cost, making it suitable for platforms with limited processing power. Subsequent works, such as F-LOAM [29], further focused on developing lightweight LOAM variants with optimized efficiency. For flat-ground scenarios, HDL-Graph-SLAM [30] employed graph optimization using NDT scan matching integrated with ground plane constraints. Ground-SLAM [31] specifically addressed structured multi-floor environments by extracting ground segments and modeling them as planar landmarks via Closest Point (CP) parameterization. Recently, KISS-ICP [32] achieved high performance through simple but effective point-to-point registration and accurate motion compensation. However, methods explicitly incorporating ground plane constraints typically assume the existence of a continuous solid ground. Additionally, ICP-based approaches, despite their computational efficiency, often overlook the richer geometric information provided by feature-based methods.

C. Semantic SLAM and Scene Understanding

Semantic SLAM commonly relies on Deep Learning (DL). SuMa++ [33] used Fully Convolutional Networks (FCNs) [34] for segmentation that allows filtering of dynamic objects. Similarly, Gong et al. [35] integrated LiDAR SLAM with a PointNet-based segmentation head to obtain semantic modeling in GNSS-denied underground parking lots. Other [36] leveraged Transformers [37] for integrated feature extraction and segmentation, enabling selective processing focused on static scene components to enhance localization accuracy. While effective for object recognition, such DL methods typically rely on large labeled datasets.

In contrast, geometric-based approaches derive semantic understanding without extensive annotations. $\mathcal{P}LC$ -LiSLAM [38] detected geometric primitives, such as planes, lines, and cylinders, as stable landmarks for SLAM optimization. Similarly, [39] achieved forest localization by clustering to identify trees and matching them to aerial canopy maps. These methods leverage inherent geometric structures for environmental understanding, avoiding the need for learned object appearance models.

D. Inland Navigation Standards and Map Integration

IENCs are vital for navigation on European inland waterways, delivering essential details on waterway layouts, aids to navigation, locks, and bridges [40]. Recent studies have explored enhancing IENCs with sensor data. For example, Van Baelen et al. [10] used onboard LiDAR to enhance situational awareness for inland vessels, detecting dynamic environments via a KDTree approach and aligning them with IENC data. Pieper and Hahn [11] proposed a 3D LiDAR sensor fusion method to improve ENC accuracy in harbor areas. Our prior work, Luo [18], dynamically updated IENCs using clustering techniques on LiDAR data. While these efforts highlight the potential of LiDAR for IENC updates, they often depend on direct projection and ad-hoc feature fitting. Similarly, Fredriksson et al. [41] converted voxel maps into 2D occupancy

grids for path planning by projecting verified free space and preserving height and slope metadata, suggesting a promising pathway for efficient 3D-to-2D map conversion. However, existing research either validates isolated ENC objects or compresses 2D maps for robotic planning, lacking an end-to-end algorithm to transform LiDAR-derived structural and semantic data into standardized geospatial overlays suitable for IENCs.

III. METHODOLOGY

A. System Overview

The Inland-LOAM framework, as shown in Figure 2, is designed to build structural semantic maps of inland waterways for enhanced situational awareness, only relying on LiDAR. The system comprises two primary modules: first, a robust LiDAR Odometry and Mapping (LOAM) pipeline for accurate pose estimation and initial environmental representation; and secondly, a semantic interpretation and conversion module to produce enhanced, IENC-compatible maps.

In the LOAM module, raw LiDAR point clouds are first continuously received by the system. These point clouds then undergo a pre-processing component to remove dynamic points from the vessel itself and to project the data onto a range image, which is a mapping in the angular coordinate, for segmentation. Next, an improved feature extraction method identifies distinct geometric features—such as surface, flat, and rough points. These features are then employed by a two-stage LiDAR Odometry component for pose estimation, which is processed further by a dedicated Plane Fitting component. Finally, the LiDAR mapping component incrementally builds the map and optimizes the trajectory. This is formulated as a factor graph optimization problem, which is solved incrementally using iSAM2 (incremental smoothing and mapping) [42] within GTSAM (the Georgia Tech Smoothing and Mapping) [43] library.

The output from the LOAM module, comprising the point cloud map and estimated poses, serves as the input for the Conversion module in Figure 2 lower part. In this module, a Voxel Map is created by dynamically combining features from the LOAM output based on probabilistic occupancy grids [44]. Next, 3D free and occupied space are identified and extracted from this Voxel Map. Slope estimation is then performed based on the extracted occupied regions. These estimated slopes, combined with local neighbourhood features from the Voxel Map, are subsequently used to determine structural semantic attributes, which collectively form a 2D Structural Semantic Map. Finally, a last conversion stage converts this 2D map into lightweight data that can be integrated with standard navigational charts.

B. System Equipment

The data acquisition setup, as illustrated in Figure 3, integrates a Robosense Helios-32 LiDAR with a Septentrio AsteRx-i3 D Pro+ GNSS/INS receiver.

In response to the inherent water-surface interference challenges of inland waterways discussed in Section II-A, Allis et al. [45] demonstrated that optimal detection of water surfaces

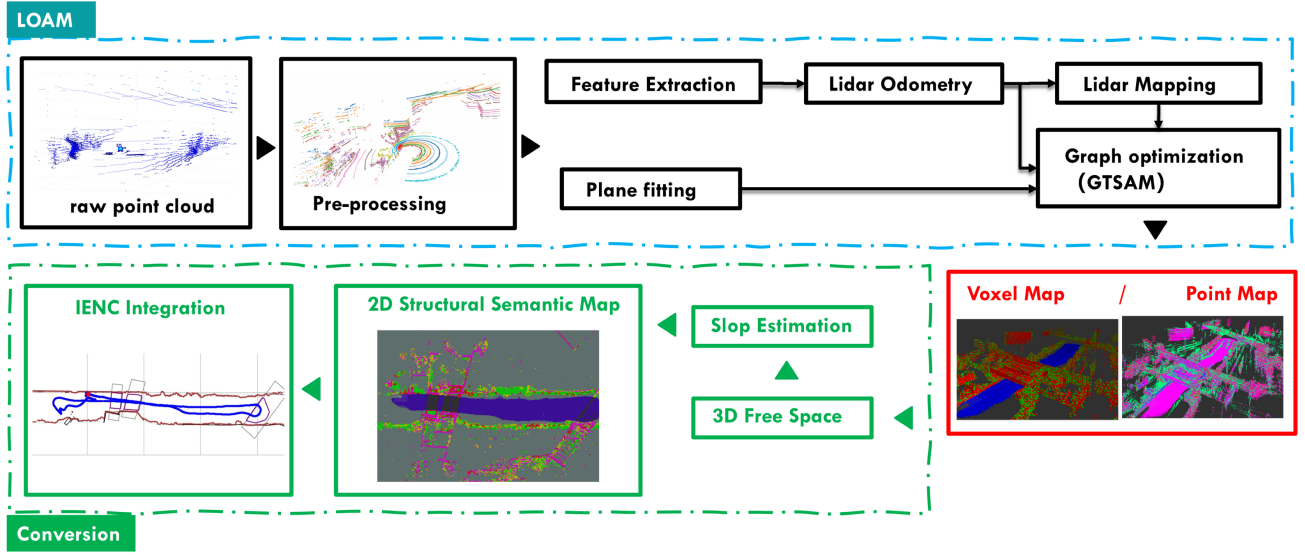


Fig. 2: Overview of the Inland-LOAM framework, which processes LiDAR data to generate IENC-compatible structural semantic maps for inland waterways. The LOAM pipeline (upper section) performs robust and low-drift LiDAR odometry. The semantic interpretation and conversion module (lower section) then uses this map to build a Voxel Map, analyze geometric properties for structural semantic understanding, and produce a 2D map converted into an IENC-compatible format.

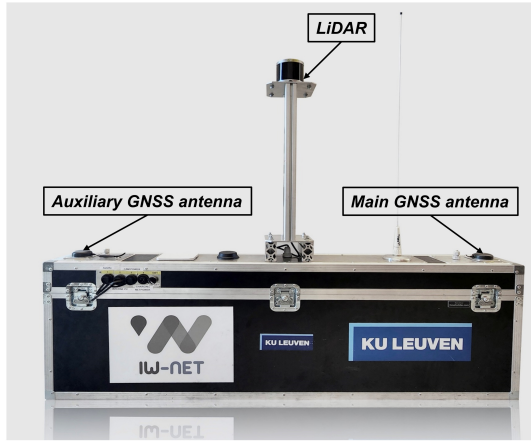


Fig. 3: The layout of sensors on our self-developed Sensor Box.

relies on diffuse reflectivity, influenced predominantly by laser incidence angles and water turbidity. Furthermore, optical constraints, such as grazing angles, inherently limit the detectable surface area. Therefore, a LiDAR with an expanded vertical field-of-view was selected to maximize the reliability of water surface detection.

The Helios-32 is 32-line LiDAR with a maximum measurement range of 150 m and an accuracy of ± 1 cm. It provides a 360 degree horizontal field of view and a 70 degree vertical FoV, characterized by a non-uniform distribution of its scan lines and an approximate vertical angular resolution of 1.33 degrees. In this paper, the LiDAR was operated at a scanning frequency of 10 Hz and a horizontal angular resolution of 0.2 degrees. The AsteRx-i3 D Pro+ GNSS/INS receiver, equipped with dual antennas and an integrated Inertial

Measurement Unit (IMU), provides acceleration and angular velocity measurements. It employs an internal Kalman filter to fuse IMU and GNSS data, delivering reliable centimeter level positioning and 3D orientation at an output frequency of 20 Hz for our experiments.

The intrinsic parameters of the IMU were calibrated using Allan Variance [46]. Extrinsic parameters calibration between the LiDAR and IMU was determined using GRIL-Calib [47]. Data processing and storage are managed by a laptop configured with an AMD Ryzen 9 PRO 7940HS CPU and 64 GB of RAM operating on Ubuntu 22.04, ROS 2¹.

C. LiDAR Odometry And Mapping Module

1) *Preprocessing and Plane Fitting*: The preprocessing begins by converting the raw LiDAR measurements into a structured range image. Let $\mathbf{P}_k = \{\mathbf{p}_i\}_{i=1}^N$ represent the LiDAR point cloud collected in the k th scan cycle, where each point $\mathbf{p}_i = [x_i, y_i, z_i]^T \in \mathbb{R}^3$ denotes spatial coordinates. Due to the substantial vertical FoV of the LiDAR and the considerable physical dimensions of the vessel, some of the LiDAR returns inevitably originate from the vessel itself. Therefore, a bounding-box ($\text{bbox}_{\text{vessel}}$) filtering step is applied to exclude these points:

$$\mathbf{P}_k^{\text{valid}} = \{\mathbf{p}_i \mid \mathbf{p}_i \notin \text{bbox}_{\text{vessel}}\}. \quad (1)$$

Given the LiDAR's non-uniform vertical distribution of its 32 laser beams and a fixed horizontal resolution of 0.2° , each scanning cycle produces a 2D range image, I_k , of dimension 32×1800 (rows \times columns). Each row corresponds to an individual laser beam, v_j represents the scan line index (row), while each column represents sequential horizontal angle increments, u_j represents the horizontal angle index (column).

¹<https://www.ros.org/>

For subsequent segmentation tasks, including water surface point separation, outlier removal, and clustering of non-surface points, the data is arranged into an information matrix representation of dimensions $32 \times 1800 \times 3$. Specifically, the three channels are configured as follows:

- **Channel 1 (Spatial Coordinates):** P_k^{valid} stores the 3D Euclidean coordinates (x, y, z) of each valid pixel (v_j, u_j) in I_k .
- **Channel 2 (Water Surface Indicator):** $M_k^{\text{surface}}(v_j, u_j)$ is a binary classification result from water surface point segmentation, marking each point as surface or non-surface.
- **Channel 3 (Cluster Labels):** $M_k^{\text{label}}(v_j, u_j)$ contains the identifiers of clusters; isolated points classified as outliers are specifically labeled.

Our system is designed for short-range localization and mapping; the curvature of the Earth can be neglected, and the water surface can be approximated as a plane [48]. Moreover, considering the limitations discussed above posed by the incidence angles of grazing on the surface of the water, the candidate points for the estimation of the plane are restricted to a predefined subset of lower LiDAR beams (N_{lines}), determined by the installation height of the LiDAR installation and the draft of the vessel.

Unlike the commonly used ground plane extraction methods [49], which iteratively ground points based on vertical angle differences between adjacent beams. For water surfaces, local geometric consistency based on angular criteria is susceptible to disruption by wave-induced undulations. RANSAC [50] is then used to fit these candidate points to the water surface plane. The estimated water surface can be mathematically described as follows:

$$\mathbf{n}_s^T \mathbf{p} + d_s = 0 \quad (2)$$

where $\mathbf{n}_s = [a_s, b_s, c_s]^T \in S^2$ is the normal vector of the plane and $d_s \in \mathbb{R}$ is its scalar offset from the sensor origin. Subsequently, any point $\mathbf{p}_j \in \mathbf{P}_k^{\text{valid}}$ is classified as a water surface point, setting the corresponding $M_k^{\text{surface}}(v_j, u_j) = 1$, if its perpendicular distance to this estimated plane, calculated as $|\mathbf{n}_s^T \mathbf{p}_j + d_s|$, is within a predefined tolerance τ_s .

The subsequent step is to segment all remaining non-surface points. The segmentation is adapted from a range image-based clustering method [51] operating on the range image I_k . For each unlabeled point, a Breadth-First Search (BFS) is initiated to find connected components. Connectivity between an active point $\mathbf{p}_{\text{current}} = \mathbf{I}_k(v, u)$ and an adjacent non-surface point $\mathbf{p}_{\text{neighbor}} = \mathbf{I}_k(v', u')$ is evaluated based on a geometric criterion. This criterion assesses the 3D spatial relationship between $\mathbf{p}_{\text{current}}$ and $\mathbf{p}_{\text{neighbor}}$ by considering their respective ranges and the angular separation between them, as specified by their pixel indices (v, u) and (v', u') and the known angular resolutions. Points are clustered into the same segment if there is no significant depth discontinuity or an overly sharp angle between them according to a threshold θ_{seg} .

All points belonging to a connected component found via BFS are assigned a unique positive integer identifier in Channel 3 (M_k^{label}). To ensure the robustness of subsequent

feature extraction, a final filtering step is applied: segments comprising fewer than 30 points are considered insignificant or noise. Points belonging to these small segments are relabeled in Channel 3 as outliers.

Algorithm 1 Feature Extraction

Require: scan: P

Ensure: feature point sets: edge \mathcal{E} , flat \mathcal{P}

Parameters: threshold: τ_1, τ_2, τ_3

```

1:  $\mathcal{E} \leftarrow \emptyset, \mathcal{P} \leftarrow \emptyset$ 
2: for all scan line  $L_k$  in  $P$  do
3:   for all segment line  $G_m$  in scan line  $L_k$  do
4:     for all point  $p_i$  in scan line  $G_m$  do
5:       Select neighbouring points:
6:        $\mathcal{M} = \{p_{i-n}, \dots, p_i, \dots, p_{i+n}\}$ 
7:       Calculate Curvature  $c_i$ 
8:        $c_i = [\frac{1}{2n} \sum_{\tilde{p} \in \mathcal{M}} (p_i - \tilde{p})]^2$ 
9:       Calculate Roughness  $r_i$ 
10:       $\bar{p} = \frac{1}{2n+1} \sum_{\tilde{p} \in \mathcal{M}} \tilde{p}$ 
11:       $r_i = \frac{1}{2n+1} \sum_{\tilde{p} \in \mathcal{M}} (\tilde{p} - \bar{p})^2$ 
12:      if  $c_i > \tau_1 \vee r_i > \tau_2$  then
13:         $\mathcal{E} \leftarrow \mathcal{E} \cup \{p_i\}$ 
14:      else if  $r_i < \tau_3$  then
15:         $\mathcal{P} \leftarrow \mathcal{P} \cup \{p_i\}$ 
16:      end if
17:    end for
18:  end for
19: end for
20: Exclude unstable points from  $\mathcal{E}, \mathcal{P}$  caused by occlusion
21: Non-maximum Suppression on  $\mathcal{E}, \mathcal{P}$ 
22: return  $\mathcal{E}, \mathcal{P}$ 

```

2) *Feature Extraction:* Our feature extraction process is similar to the method in [16], but with optimized roughness characterisation for structural semantic mapping. Features are extracted from the segmented ground planes and surfaces identified in the preceding clustering step. A key challenge involves the robust discrimination of surface texture characteristics at local regions.

Traditional approaches often extract features based on local range differences. For instance, a common metric (Equation 3, where $|L|$ is the size of the local neighborhood, e.g., 10 points, and r_i is the range of point i) is:

$$c = \frac{1}{|L| \cdot \|r_i\|} \left\| \sum_{j \in L, j \neq i} (r_j - r_i) \right\| \quad (3)$$

While this method is computationally efficient and applicable to all directions, it demonstrates limitations in inland waterway environments. In areas with dense vegetation, grass, or gravel, the local surface exhibits numerous small, "edge-like" bumps. When applying Equation 3, the positive and negative range residuals $(r_j - r_i)$ from neighboring points p_j on either side of the central point p_i tend to cancel each other out.

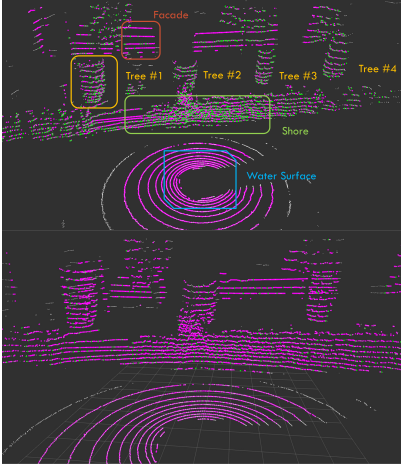


Fig. 4: Comparative performance of feature extraction. Purple points indicate planar features, while green points denote rough features. The upper figure illustrates the feature distribution by our method, where semantic information of the targets is annotated, including building facades, trees, shore, and water surface. Notably, the shore is largely covered by vegetation, with only a small portion appearing as a flat surface. The lower figure shows the feature distribution of LOAM-based methods.

Consequently, such curvature estimations often overlook subtle surface textures and primarily respond only to more extreme geometric features like significant peaks or occlusions.

To overcome this limitation and effectively capture local surface roughness, thereby distinguishing between smooth and textured surfaces, we employ a variance-based approach to quantify local range variations as detailed in Algorithm 1. Figure 4 illustrates the comparative performance of feature extraction between LOAM-based methods and our optimized approach.

3) LiDAR Odometry, Mapping and Joint Optimization:

Our LiDAR odometry and mapping parts build upon LeGO-LOAM [16], with specific adaptations in Joint Optimization. The system employs a two-stage registration process for pose estimation, integrating water surface constraints. The overall factor graph structure is illustrated in Figure 5.

Two-Stage LiDAR Odometry: a two-step Levenberg-Marquardt optimization to estimate the transformation between consecutive scans. First, the planar features \mathcal{F}_p^t extracted from the water surface and other planar environmental elements are matched to their correspondences using a point-to-plane association in \mathcal{F}_p^{t-1} to determine $[t_z, \theta_{roll}, \theta_{pitch}]$. Then, the remaining transformation parameters $[t_x, t_y, \theta_{yaw}]$ are estimated using edge features \mathcal{F}_e^t matched against \mathcal{F}_e^{t-1} through a point-to-line association [15], while applying the previously computed vertical and angular parameters as constraints, resulting in the full 6 DoF transformation. This decoupled registration method significantly reduces computation time and is well-suited to our edge computing scenario.

LiDAR Mapping: To refine pose estimation, the LiDAR mapping module matches the extracted features $\{\mathcal{F}_e^t, \mathcal{F}_p^t\}$ to a surrounding point cloud map at a lower frequency than the odometry module. Unlike the original LOAM that maintains

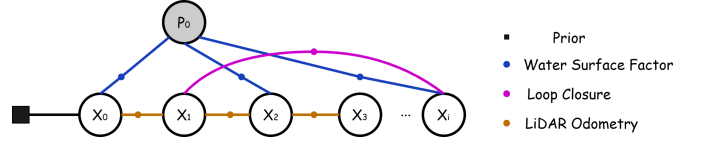


Fig. 5: Inland-LOAM factor graph structure, showing prior, water surface, LiDAR odometry, loop closure factors.

a single point cloud map, we store individual feature sets $\{\mathcal{F}_e^t, \mathcal{F}_p^t\}$ along with their corresponding poses. The surrounding map is constructed by transforming and fusing feature sets whose poses are within the sensor's field of view (typically within 100m of the current position). This strategy of storing discrete feature sets with their poses facilitates flexible factor graph optimization. The resulting odometry estimates provide a continuous trajectory of the vessel. However, as with any LiDAR-based odometry, these estimates accumulate drift over time, particularly along the vertical axis due to the typical scarcity of distinct, stable horizontal features in many inland waterway environments.

Joint Optimization with Water Surface Constraints: The water surface provides a globally reference plane, ideal for mitigating drift that accumulates over long trajectories. Unlike the fragmented planar features typically found in terrestrial environments, the vast and continuous nature of the water surface offers a simple but effective constraint. To take advantage of this, we introduce the water surface constraint into the factor graph optimization framework. We parameterize the water surface as a globally consistent plane P_w with parameters $\{\mathbf{n}_w, d_w\}$ as defined in Equation 2.

The objective of our estimation is to determine the optimal set of robot poses $\mathcal{T} = \{T_k\}_{k=0}^N$, where $T_k \in SE(3)$. This is achieved by minimizing a cost function composed of several weighted squared error terms, representing the negative log-likelihood of the measurements given the states and plane parameters. The optimization problem is formulated as finding $\mathcal{X}^* = \{\mathcal{T}^*, P_w^*\}$ by minimizing:

$$\begin{aligned} \mathcal{X}^* = \arg \min_{\mathcal{T}, P_w} & \|r_0\|_{\Sigma_0}^2 \\ & + \sum_k \|r_{\text{odom},k}(T_k, T_{k+1})\|_{\Sigma_{\text{odom},k}}^2 \\ & + \sum_{(i,j) \in \mathcal{L}} \|r_{\text{loop},ij}(T_i, T_j)\|_{\Sigma_{\text{loop},ij}}^2 \\ & + \sum_{m \in \mathcal{M}} \|r_{\text{plane},m}(T_m, P_w)\|_{\Sigma_{\text{plane},m}}^2 \end{aligned} \quad (4)$$

In this formulation, $\|r\|_{\Sigma}^2$ denotes the squared Mahalanobis distance $r^T \Sigma^{-1} r$, where Σ is the covariance matrix of the corresponding residual r . The term r_0 represents a combined prior residual on initial knowledge about the system, such as the initial pose T_0 or an initial estimate for the plane, with Σ_0 as its covariance. The odometry residual, $r_{\text{odom},k}$, for the relative motion $\Delta \tilde{T}_{k,k+1}$ measured between consecutive poses T_k and T_{k+1} , is given by

$$r_{\text{odom},k} = \text{Log}((\Delta \tilde{T}_{k,k+1})^{-1} (T_k^{-1} T_{k+1})) \in \mathbb{R}^6, \quad (5)$$

where $\text{Log}(\cdot)$ maps an $SE(3)$ element to its tangent space representation. Similarly, the loop closure residual $r_{\text{loop},ij}$, constrains the measured relative transform $\Delta\tilde{T}_{i,j}$ between non-consecutive poses T_i and T_j . This transform is computed using ICP [52] to verify a potential match between keyframes, and the resulting constraint is added to a pose graph optimized by iSAM2 [42]. Note that only the experiment in area A uses this technique. The residual (where $(i,j) \in \mathcal{L}$ denotes the set of loop closures) is defined as

$$r_{\text{loop},ij} = \text{Log}((\Delta\tilde{T}_{i,j})^{-1} (T_i^{-1}T_j)) \in \mathbb{R}^6. \quad (6)$$

The sum $\sum_{m \in \mathcal{M}}$ accounts for all water plane observations, where \mathcal{M} is the set of keyframes with such observations.

The water plane residual, $r_{\text{plane},m}(T_m, P_w)$, arises from observing the water surface at a keyframe with pose $T_m = (R_m, t_m)$. A local plane $P_{s,m} = (n_{s,m}, d_{s,m})$ is measured in the sensor frame, satisfying

$$n_{s,m}^\top x_s + d_{s,m} = 0. \quad (7)$$

This locally observed plane is transformed into the global coordinate frame by T_m to obtain a predicted global plane observation $\hat{P}_{w,m} = (\hat{n}_{w,m}, \hat{d}_{w,m})$. The predicted global normal is

$$\hat{n}_{w,m} = R_m n_{s,m}, \quad (8)$$

and the predicted global offset is derived from the transformed plane equation

$$(R_m n_{s,m})^\top x_w + (d_{s,m} - (R_m n_{s,m})^\top t_m) = 0, \quad (9)$$

which gives

$$\hat{d}_{w,m} = d_{s,m} - (R_m n_{s,m})^\top t_m. \quad (10)$$

The residual then compares the estimated global plane $P_w = (n_w, d_w)$ with this transformed local observation $\hat{P}_{w,m}$. Using an error operator \ominus the operator that defines the error between two planes($P_w, \hat{P}_{w,m}$), then:

$$\begin{aligned} r_{\text{plane},m}(T_m, P_w) &= P_w \ominus \hat{P}_{w,m} \\ &= \begin{pmatrix} e_N(n_w, \hat{n}_{w,m}) \\ d_w - \hat{d}_{w,m} \end{pmatrix} \\ &= \begin{pmatrix} e_N(n_w, R_m n_{s,m}) \\ d_w - (d_{s,m} - (R_m n_{s,m})^\top t_m) \end{pmatrix} \in \mathbb{R}^3. \end{aligned} \quad (11)$$

Here, $e_N(n_w, \hat{n}_{w,m}) \in \mathbb{R}^2$ is the 2D error vector representing the difference in orientation between the global plane normal n_w and the predicted global normal $\hat{n}_{w,m}$ from the measurement. This error is typically computed by first defining a 3D error vector $\hat{\xi}$ in the tangent space of n_w , defined as follows:

$$\hat{\xi} = -\frac{\arccos(n_w^\top \hat{n}_{w,m})}{\sqrt{1 - (n_w^\top \hat{n}_{w,m})^2}} (\hat{n}_{w,m} - (n_w^\top \hat{n}_{w,m}) n_w), \quad (12)$$

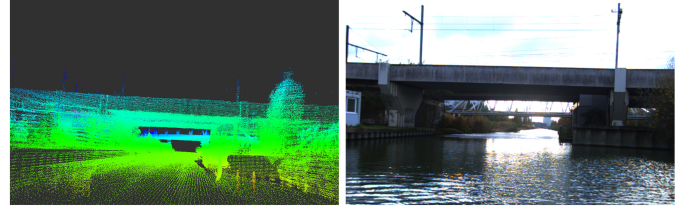


Fig. 6: The left image presents the point cloud map generated by our method in this scenario, while the right image shows the corresponding camera image captured in the same scene.

Then, the error e_N is then obtained by projecting $\hat{\xi}$ using the basis B_{n_w} :

$$e_N(n_w, \hat{n}_{w,m}) = B_{n_w}^\top \hat{\xi}. \quad (13)$$

Here, $B_{n_w} \in \mathbb{R}^{3 \times 2}$ is a matrix whose columns form an orthonormal basis for the 2D tangent space at the point n_w on the unit sphere S^2 .

By leveraging the water surface as a global geometric constraint, our approach reduces vertical drift, as visualized in Figure 6.

D. Structural Semantic Map Conversion

1) *Semantic voxel transformation*: In the preceding section, a map comprising structured point cloud features was generated. Each point in this cloud has been classified with semantic labels, including the water surface, flat points, or rough points. To efficiently store and query this semantic information within the global map, the "dense" semantically annotated point cloud is transformed into a "sparse" voxel grid representation. For each voxel, a probabilistic estimate of its semantic terrain class is maintained. This is achieved by adapting the log-odds update mechanism, commonly used in probabilistic occupancy grids [44], to instead fuse evidence over time for competing semantic labels.

The workspace is discretized into a 3D voxel grid with a uniform resolution r , set to 0.15 m in this work. This resolution is chosen considering a balance between memory consumption, computational efficiency, and the typical scale of objects of interest in inland waterways. The entire transformation process is depicted in Figure 7. For each voxel v_i , we maintain a hash map to store its semantic state $S(v_i)$. This state involves accumulating evidence for the semantic classes: water surface, flat terrain, and rough terrain. The 'unknown' category is assigned if a voxel has insufficient evidence for any specific class.

Points pre-classified as water surface by the LiDAR odometry module are handled directly, if such a point falls into voxel v_i , the voxel is immediately assigned the "water" semantic label with high confidence.

For terrain characteristics, we maintain log-odds values within the hash map entry for each non-water voxel. The initial belief for each of these log-odds components in every newly considered voxel is denoted as $l_{0,i}$.

When a new semantic point p_t observed at time t , belonging to a terrain class $c \in \{\text{flat}, \text{rough}\}$, falls within voxel v_i , the log-odds for that class in the voxel is updated as follows:

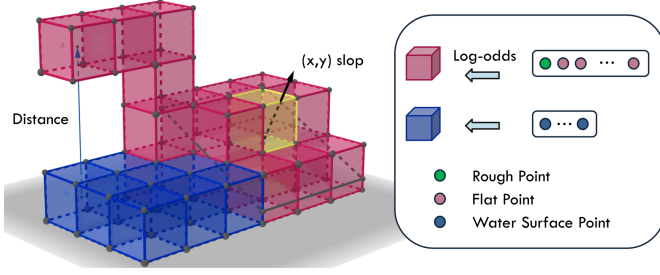


Fig. 7: Overview of the Structural Semantic Map Conversion. Red voxels represent non-water voxels, while blue voxels indicate water voxels. During the transformation process, rough and planar points are accumulated as log-odds values and ultimately classified into three semantic categories: flat, rough, or unknown. Water voxels directly inherit the water surface points from the point cloud. The voxel map further supports slope estimation and bridge clearance calculation. For slope estimation, the yellow voxel represents the target cell, and a square neighborhood window is used for local slope computation. Bridge clearance is determined by measuring the vertical distance from the water surface voxels to the nearest non-water voxels above.

$$l_{t,i}^c = \text{logit}(p(m^c|y_t)) + l_{t-1,i}^c - l_{0,i}^c \quad (14)$$

where the log-odds in voxel v_i at time t is $l_{t,i}^c$. The term $p(m^c|y_t)$ represents the probability of observing class c given the measurement y_t . The logit function is defined as $\text{logit}(p) = \ln\left(\frac{p}{1-p}\right)$. We define the observation model probabilities for semantic classes, $p(\text{flat}) = p_f$ (e.g., $p_f = 0.7$) and $p(\text{rough}) = 1 - p_f$.

Following the update, the log-odds l_i^c for each voxel v_i and each class c are converted back to probabilities:

$$P_i^c = \sigma(l_i^c) = \frac{1}{1 + e^{-l_i^c}} \quad (15)$$

Ultimately, each voxel v_i is assigned a definitive semantic label. Based on the probability, P_i^c :

$$S(v_i) = \begin{cases} \text{"flat"} & \text{if } P_i^{\text{flat}} - 0.5 > \tau_{\text{flat}} \\ \text{"rough"} & \text{if } P_i^{\text{flat}} - 0.5 < -\tau_{\text{rough}} \\ \text{"unknown"} & \text{otherwise} \end{cases}$$

2) *2D structural semantic map construction*: The 3D semantic voxel map is subsequently projected onto a unified 2D structural semantic map. While it refers on the conversion method [41], this variant targets USV rather than UGV/UAV scenarios and adopts different map architectures for refined slope estimation and richer semantic inference. To effectively map the complex environment encountered by USVs in inland waterways, this framework broadly classifies non water surface areas into four structural semantic categories. These are: *Horizontal Planar Surfaces* (HP), which include water surface, level terrain, and flat artificial or natural shore platforms; *Vertical Planar Surfaces* (VP), encompassing the facades of structures like bridges, buildings, and vessels, as well as vertical embankments; *Complex Horizontal Terrain*

(CH), referring to irregular embankments, grasslands and low-lying scrub; and *Complex Vertical Structures* (CV), representing non-planar, upright natural elements like trees and dense bankside vegetation. Additionally, two further categories are defined for features on and over the water: *Open Water Surface* (OW) and *Under Bridge Clearance Zone* (UB), which identify the safe, traversable area beneath bridge structures.

The foundation of this conversion is an intermediate 2D grid representation, where each cell (x, y) retains detailed information regarding the vertical distribution of voxels and their semantic labels derived from the 3D voxel map. Specifically, for each cell (x, y) at the defined map resolution, we consider the voxel set: $V_{xy} = \{(z_j, s_j, p_j^{\text{orig}})\}_{j=1}^{N_{xy}}$ where z_j is the voxel height, s_j is the semantic label (e.g., water, flat, rough and unknown), p_j^{orig} denotes the original 3D coordinates, and N_{xy} is the total number of voxels in the vertical column at (x, y) . For outdoor environments lacking explicit ceilings, the local maximum voxel height Z_{\max} serves as an initial estimate for the upper boundary of free space above newly detected occupied regions.

The next step is to perform slope estimation on these voxel sets, as illustrated in Figure 7. In contrast to methods that derive slope using only boundary heights, our approach calculates the slope through all voxel points within a defined local neighbourhood. This method is more suitable for estimating those structures such as VP, CV, or overhangs.

For a target cell (x_c, y_c) , we define a square neighborhood window W_{xy} of size $(2S_a + 1) \times (2S_a + 1)$, where S_a specifies the extent of the neighbourhood.

Each voxel in W_{xy} is represented by its relative coordinates and height $(x_k^{\text{rel}}, y_k^{\text{rel}}, z_k)$, measured with respect to (x_c, y_c) . Let N be the total number of such voxel data points aggregated from all cells within the entire window W_{xy} . The slope estimation is then performed using a least squares fit of a plane. The plane fitting is formulated as:

$$\underbrace{\begin{bmatrix} x_1^{\text{rel}} & y_1^{\text{rel}} & 1 \\ x_2^{\text{rel}} & y_2^{\text{rel}} & 1 \\ \vdots & \vdots & \vdots \\ x_N^{\text{rel}} & y_N^{\text{rel}} & 1 \end{bmatrix}}_A \underbrace{\begin{bmatrix} a \\ b \\ c \end{bmatrix}}_{\theta} = \underbrace{\begin{bmatrix} z_1 \\ z_2 \\ \vdots \\ z_N \end{bmatrix}}_B. \quad (16)$$

The parameters $\theta_{\text{ls}} = [a, b, c]^T$ defining the best-fit plane are determined by solving the linear least squares problem shown in Eq. (16). To ensure numerical stability, the solution is obtained by computing the Moore–Penrose pseudoinverse A^+ of A via singular value decomposition (SVD), rather than by explicitly forming normal equations.

$$\theta_{\text{ls}} = A^+ B, \quad (17)$$

Subsequently, the slope m_{xy} at the central cell (x_c, y_c) is computed as:

$$m_{xy} = \sqrt{a_{\text{ls}}^2 + b_{\text{ls}}^2}. \quad (18)$$

The structural label for each 2D grid cell is determined by comparing three cues— N (the number of reliable voxels in the window); R_{plane} (the fraction of those voxels that belong to

locally planar surfaces $R_{\text{plane}} = \frac{N_{\text{plane}}}{N_{\text{total}}}$); and the local slope m_{xy} . Let $\{N_{\text{low}}, N_{\text{high}}\}$, $\{R_{\text{low}}, R_{\text{high}}\}$, and $\{m_{\text{low}}, m_{\text{high}}\}$ denote a set of heuristic rules. A cell is classified as:

- **HP (Horizontal Plane)** if $N > N_{\text{high}}$, $R_{\text{plane}} > R_{\text{high}}$ and $m_{xy} < m_{\text{low}}$;
- **VP (Vertical Plane)** if $N > N_{\text{low}}$, $R_{\text{plane}} > R_{\text{low}}$ and $m_{xy} > m_{\text{high}}$;
- **CH/CV (Complex Horizontal / Vertical)** whenever the slope is appreciable ($m_{xy} \geq m_{\text{low}}$) but the planar support is insufficient for VP or HP;

A grid cell that contains only water-labelled voxels is marked as *Open Water* (OW). If a second, non-water voxel layer appears more than a predefined safety margin τ_{bridge} (e.g., 3.0m) above the water layer, the cell is flagged as *Under-Bridge* (UB) the vertical clearance, G_{bridge} is determined by the difference $G_{\text{bridge}} = Z_{\text{overhead_lowest}} - Z_{\text{water_level}}$, where $Z_{\text{overhead_lowest}}$ is the Z-axis of the lowest point of the overhead structure and $Z_{\text{water_level}}$ represents the Z-axis of the highest point water surface within the vertical column. These additional rules override the geometric label whenever they trigger, ensuring bridges are never misclassified.

To provide a more practical representation of the clearance under the bridge, we first divide the 2D grid map into local blocks of size $l \times l$ and compute the mean and range of G_{bridge} within each block. These blocks are then further grouped into larger contiguous regions using BFS. For each region, the mean clearance of its constituent blocks is taken as the representative value, so that each under-bridge area is assigned a single vertical clearance. This two-stage aggregation ensures both the accuracy and real-time performance of the measurement.

3) *Generation of IENC Compatible Map*: This process transforms costmap data into a durable and shareable representation, aiming for compatibility with IENC standards. It involves extracting key features, such as shorelines and bridges, and representing them with distinct geometric primitives. The method begins by encoding specific occupancy categories into an RGB image where each category is assigned a unique color value. Subsequently, two primary types of features are extracted, detailed in Algorithm 2.

For **Shoreline Extraction Represented by Points**, a ray casting method is used to delineate shorelines. From the boundaries of identified water regions, rays are projected outwards in multiple directions. The end points of these rays, where they intersect the nearest non-water pixels, define the shoreline.

For **Bridge Extraction Represented by Polygons**, bridge pixels are first identified and then clustered using DBSCAN [53] to group fragmented detections into coherent structures. For each cluster, a convex hull is computed to generate a polygonal representation. Overlapping or closely spaced polygons are merged to ensure continuous bridge structures are represented as unified entities. The resulting polygons are then exported in JSON format for integration with navigation systems.

Algorithm 2 Costmap \rightarrow IENC Feature Extraction

Require: RGB image \mathcal{I}

Ensure: Shoreline points $\mathcal{S}_{\text{shore}}$, bridge polygons \mathcal{B}

Parameters: DBSCAN (ε , n_{min}), hull merge distance δ , ray step s , angle step $\Delta\theta$

// ———— Shoreline extraction ————

1: Define \mathcal{B}_w : set of water boundary pixels in \mathcal{I}

2: Define \mathcal{O} : set of obstacle mask pixels in \mathcal{I}

3: Define \mathcal{Q} : set of shoreline hit

4: $\mathcal{Q} \leftarrow \emptyset$

5: **for all** $p_0 \in \mathcal{B}_w$ **do**

6: **for** $\theta = 0$ **to** $360 - \Delta\theta$ **step** $\Delta\theta$ **do**

7: **for** $k = 1$ **to** max_steps **do**

8: $\mathbf{p} \leftarrow p_0 + k \cdot s \cdot (\cos \theta, \sin \theta)^T$

9: **if** \mathbf{p} is out of bounds **then**

10: **break**

11: **end if**

12: **if** \mathbf{p} is not water **then**

13: **if** \mathbf{p} is obstacle **then**

14: $\mathcal{Q} \leftarrow \mathcal{Q} \cup \{\mathbf{p}\}$; **break**

15: **else**

16: **break**

17: **end if**

18: **end if**

19: **end for**

20: **end for**

21: **end for**

22: $\mathcal{S}_{\text{shore}} \leftarrow \text{DOWNSAMPLE}(\mathcal{Q})$

// ———— Bridge extraction ————

23: Define $\mathcal{P}_{\text{bridge}}$: set of bridge pixels in \mathcal{I}

24: labels $\leftarrow \text{DBSCAN}(\mathcal{P}_{\text{bridge}}, \varepsilon, n_{\text{min}})$

25: Initialize set of bridge polygons

26: $\mathcal{H} \leftarrow \emptyset$

27: **for** each cluster C in labels **do**

28: $\mathcal{H} \leftarrow \mathcal{H} \cup \{\text{CONVEXHULL}(C)\}$

29: **end for**

30: Merge polygons within δ distance

31: $\mathcal{B} \leftarrow \text{MERGEINTERSECTING}(\mathcal{H}, \delta)$

32: **return** $\mathcal{S}_{\text{shore}}, \mathcal{B}$

IV. EXPERIMENTS AND DISCUSSION

A. Data Collection

To validate the performance of the proposed Inland-LOAM, we conducted three representative experiments on November along [the canal from Leuven to the Dijle](#) (50°53.8890'N, 004°42.4010'E). The test routes span various conditions, including urban canyons, vegetated banks, mooring zones, and bridge crossings, providing a challenging and realistic testbed for evaluating the robustness and precision of our semantic mapping and localization system.

Data were collected using a catamaran named the Maverick, with an overall length of 6.10 m and a beam of 2.02 m, as illustrated in Figure 1. Its draft varies from approximately 0.30 m (lightskip) to 0.60 m (fully ballasted). The twin-hull configuration provides inherent stability, beneficial for sensor

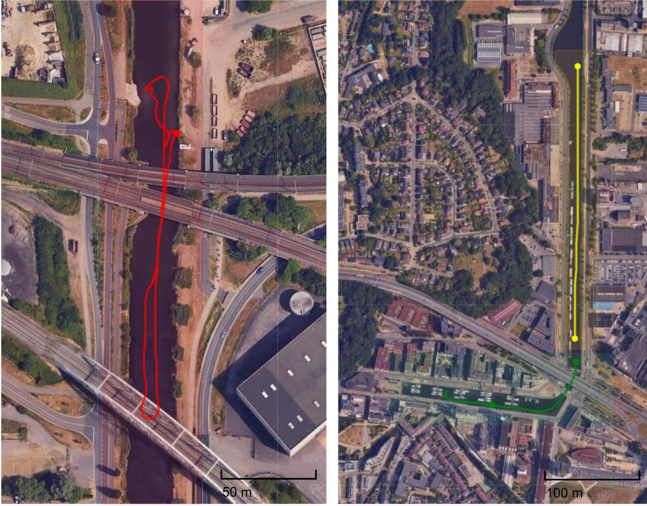


Fig. 8: Our data collection was conducted along the canal from Leuven to the Dijle. The collected trajectories are visualized as follows: Area A in red, Area B in yellow, and Area C in green.

data acquisition. The vessel was equipped with the sensor suite detailed in Section III-B.

We recorded three datasets along this route, as shown in Figure 8, to cover different typical inland waterway environments and to demonstrate the semantic mapping capability. These trajectories are named as follows, listed in Table I:

- **Mixed Area:** Between two fixed bridges, with quay walls, stone revetments, vegetated banks, and exposed soil.
- **Vegetation Area:** Both banks are densely vegetated, featuring several mooring facilities and multiple docked vessels.
- **Urban Port Area:** There are large buildings on both sides of the Port, including a fixed bridge and a lifting bridge, with multiple mooring facilities and small boats docked.

TABLE I: Our Inland Waterway Datasets

Experiment	Distance [m]	Duration [s]	Loop Back	Weather
A (Mixed Area)	424.5	561.7	✓	Sunny
B (Vegetation Area)	583.5	356.8	✗	Overcast
C (Urban Port Area)	474.9	399.9	✗	Overcast

B. Evaluation of Trajectory and Point Cloud Mapping

To highlight the performance of our method, we conducted comparative experiments against several state-of-the-art methods: KISS-ICP, HDL-SLAM, LeGO-LOAM, and LOAM. To ensure a fair and consistent comparison, all methods were adapted to match the laser beam distribution specific to our dataset. Specifically for HDL-SLAM, we configured it for odometry-only with planar constraints enabled.

To assess the quality of the generated point cloud maps, we compared Inland-LOAM visually with LOAM, LeGO-LOAM, HDL-SLAM, and KISS-ICP within Area B, as illustrated in Figure 9. The gradient coloring along the trajectory indicates

elevation changes. Notably lacking bridges or large overhead structures, Area B presents a challenge for evaluating vertical localization accuracy.

At a global scale, LOAM and KISS-ICP show a water surface that curves downwards along the z-axis, while HDL-SLAM exhibits an upward curvature. In contrast, LeGO-LOAM displays only minor z-axis drift. Inland-LOAM maintains a relatively flat water surface, demonstrating superior mitigation of vertical drift. At a local scale, Figure 9 details the mapping quality of the same building produced by each method, reflecting the precision of their horizontal registration. KISS-ICP, LOAM, and LeGO-LOAM fail to reconstruct the building’s windows, capturing only the main facade. While HDL-SLAM correctly identifies the windows, it fails to represent their proper alignment. However, Inland-LOAM accurately reconstructs both the windows and their correct spatial arrangement, a clear benefit of our optimized feature extraction algorithm.

The accuracy of the trajectory estimation was quantitatively assessed by comparing Inland-LOAM with LOAM, LeGO-LOAM, KISS-ICP, and HDL-SLAM. Figure 10 presents these comparative trajectories. We calculated the Root Mean Square Error (RMSE) and Standard Deviation (STD) between RTK-GNSS ground truth positions and the trajectories generated by these methods, as summarized in Table II. It is important to note that, although RTK-GNSS data were treated as ground truth, GNSS signals can experience drift in certain inland waterway scenarios, particularly under bridges or in narrow urban sections in Figure 10a (sections 1 and 2) and Figure 10c (right side).

As shown in Figure 10b, the Inland-LOAM trajectory closely aligns with the RTK-GNSS ground truth, while other methods exhibit a noticeable gap. In Figure 10a and 10c, HDL-SLAM and KISS-ICP display a larger gap, while Inland-LOAM consistently maintains a minimal deviation from the ground truth. Regarding the Z-axis comparison, Inland-LOAM demonstrates the lowest error in all scenarios. Notably, in Figure 10a, the Z-axis trajectory of LeGO-LOAM is similar to that of Inland-LOAM, unlike significant errors from other scenarios. The primary reason is that Area A contains multiple bridges; those overhead structures provide strong geometric observations that reduce the degeneracy of the Z-axis estimation. As shown in Table II, Inland-LOAM achieves the lowest RMSE and standard deviation in each test case. In particular, in Area A, the loop closure module had a negative effect, resulting in a higher RMSE compared to the odometry-only version. We attribute this to the highly similar scenery of the narrow waterway, which likely caused false positive loop closures, introducing errors that outweighed the accumulated odometry drift. Overall, the trajectory results indicate that although all methods performed similarly in general localization within inland waterways, Inland-LOAM achieved superior accuracy and robustness under challenging conditions. This high-precision trajectory estimation provides a solid foundation for subsequent semantic analysis and mapping tasks.

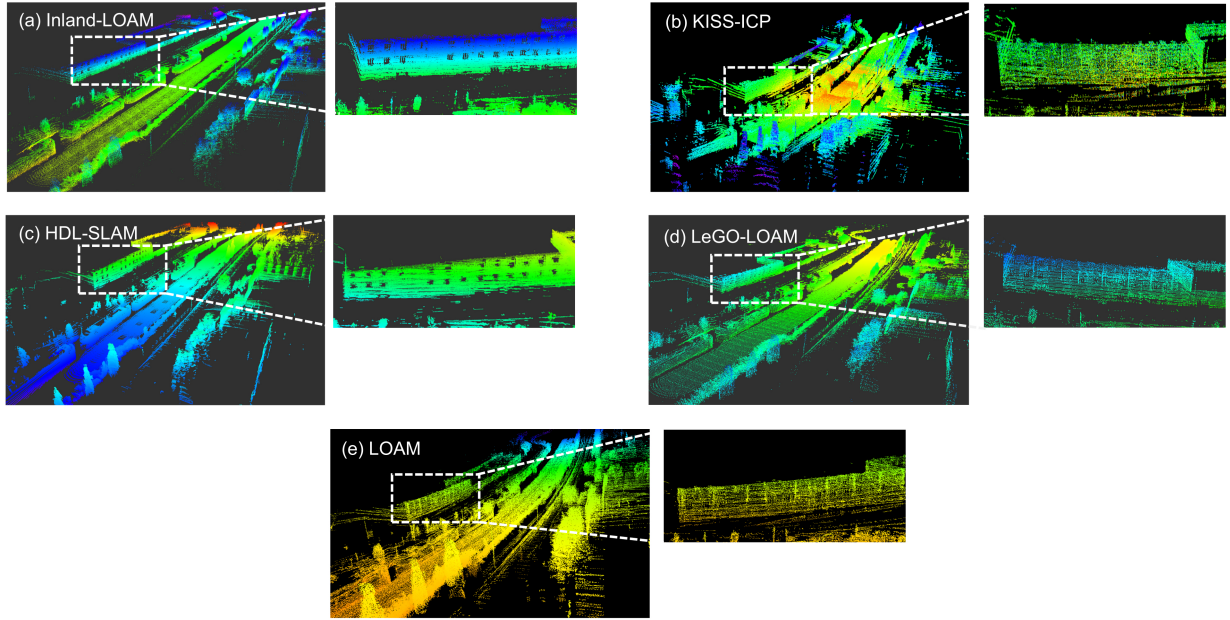


Fig. 9: Mapping results of Inland-LOAM, KISS-ICP, HDL-SLAM, LeGO-LOAM, and LOAM in the vegetation area, with a building detail by each method in this scene. The gradient coloring in the Z-axis direction indicates elevation changes.

TABLE II: Algorithm trajectory accuracy evaluation.

Seq	Inland-LOAM		Inland-LOAM*		HDL-SLAM		HDL-SLAM*		KISS-ICP		LeGO-LOAM		LeGO-LOAM*		LOAM	
	RMSE	STD	RMSE	STD	RMSE	STD	RMSE	STD	RMSE	STD	RMSE	STD	RMSE	STD	RMSE	STD
A	0.45	0.37	0.49	0.39	3.13	1.34	3.14	1.34	1.28	0.64	0.48	0.37	0.77	0.55	1.27	0.58
B	0.60	0.30	-	-	4.87	2.11	-	-	9.61	4.78	2.26	1.14	-	-	7.44	3.59
C	0.99	0.72	-	-	2.25	1.06	-	-	2.22	1.08	2.01	0.83	-	-	1.97	0.97
Avr	0.68	0.46	-	-	3.42	1.50	-	-	4.37	2.17	1.58	0.78	-	-	3.56	1.71

*Variant with the loop closure module activated.

C. Structural Semantic Mapping Evaluation

This section evaluates the quality of these semantic maps and discusses their practical utility. We assess the performance of our method by comparing the generated structural semantic maps with their real-world counterparts.

Figure 11 presents the 2D structural semantic maps generated for our three experimental areas A, B, and C. Figure 11a shows the performance along an inland waterway with highly diverse shoreline characteristics. The system accurately identifies navigable areas under bridges, providing real-time bridge clearance estimations (H-1, H-2, H-3), which are essential for the safe passage of large vessels and address the limitations of traditional static IENCs. Furthermore, it demonstrates the ability to differentiate shoreline constructions, distinguishing boat ramps classified as HP at c-1, shore platforms (HP) at e-3, containers classified as VP at d-2, and bridge piers (VP) at e-1. It also distinguishes vegetated banks classified as CH and CV at a-2, and piling identified as CV at c-2.

Figure 11b illustrates a scenario dominated by dense reed vegetation. The map correctly captures the overall characteristics of the canal, categorizing large buildings at location b-1 as VP and most of the shoreline as complex terrain CH or CV, aligning well with real-world scenes. However, this

scenario highlights limitations of purely geometric classification. Scattered small HP and VP regions appear within extensively classified vegetation areas (e.g., near c-2 and d-2). Such ambiguity likely results from LiDAR penetrating sparse foliage and capturing flat ground or mistaking dense, flat-topped vegetation as planar surfaces. Although this reveals the inherent challenges of using geometric methods in complex natural environments, it also demonstrates the ability to detect subtle variations in surface structure.

In Figure 11c, the system successfully identifies bridges and labels the navigable water beneath UB. It clearly classifies large building facades in b-3 as VP, and precisely outlines vessels (b-2, c-2) and revetments (b-1, c-1). However, movement of the lifting bridge (H-1) during data acquisition led to color mixing between the UB and VP areas, revealing limitations of our system in dynamic environments.

These semantic maps represent not only geometric reconstructions but also serve as costmaps directly usable for navigation planning. For USV decision-making, the OW regions represent low-cost navigable areas, while the UB areas indicate regions requiring height awareness. Combined HP and VP regions, such as docks, can be considered potential docking platforms. Continuous VP boundaries adjacent to OW can in-

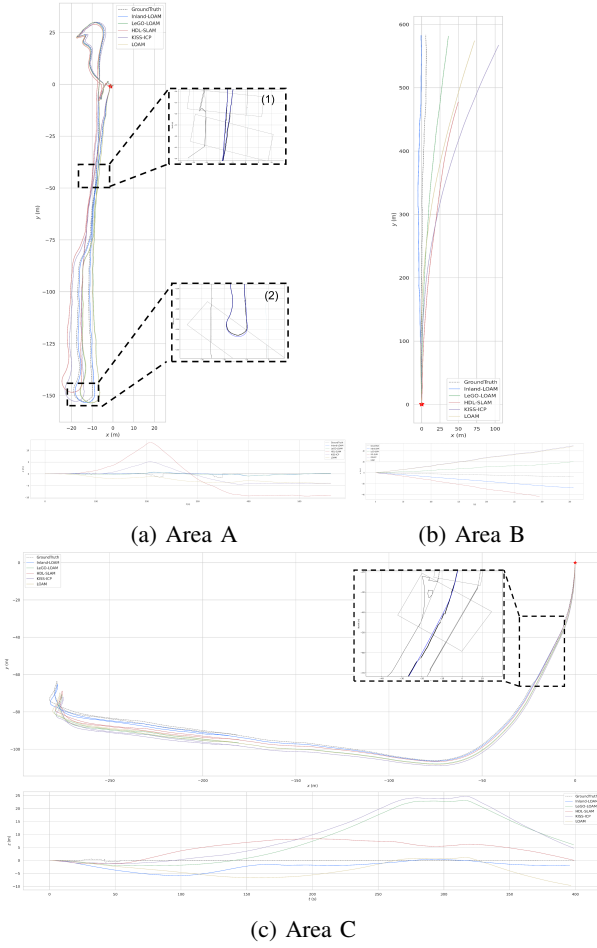


Fig. 10: Trajectory comparison of all evaluated algorithms against the ground truth. The main plots compare the estimated trajectories against the ground truth in both horizontal and vertical dimensions, with each trajectory only aligned with the ground truth at the origin point. Sub-figures (a-1), (a-2), and the right of (c) project the Inland-LOAM (blue) and ground truth (black) trajectories onto IENC to demonstrate accuracy in confined spaces, after rigidly aligning Inland-LOAM to the ground truth.

dicade vessel or revetment boundaries, whereas VP boundaries distant from OW can represent building facades for higher-level semantic localization tasks. The CH and CV regions represent high-cost obstacles or areas that require careful avoidance to prevent grounding or vegetation entanglement of engines.

D. Shoreline Boundaries Comparison with Reference Maps

To evaluate the effectiveness of the boundaries derived from structural semantic mapping, we performed a comparative analysis with three widely used reference maps: Google Earth, OpenStreetMap (OSM)², and IENCs. As illustrated in Figure 12, each reference map was created using data from a different period: Google Earth used aerial imagery from on or before June 16, 2023; OSM is based on a continuously

updated database; and the IENC data was last modified on July 1, 2021.

In Area A (Figure 12a), shoreline boundaries (red hits) align with the contours of artificial structures such as revetments and shoreline constructions, exhibiting strong correspondence with the IENC and Google Earth. In contrast, for vegetated banks, some discrepancies appear relative to the satellite imagery, reflecting seasonal variation in reeds or minor erosion not represented in the static maps. In Area B (Figure 12b), our system accurately delineates boundaries, including vessels moored long-term along the canal. Area C (Figure 12c) demonstrates a distinct case. Although the canal boundary aligns with all reference datasets, the layout of moored vessels within the port basin shows a notable divergence. The positions identified by Inland-LOAM are consistent with the latest updates in OSM and differ from the outdated layouts present in other map, reflecting Inland-LOAM's potential to dynamically enhance and maintain up-to-date navigational charts.

E. Time analysis

Table III evaluates the real-time performance of the LOAM module. The front-end components, which include pre-processing, plane fitting, feature extraction, and LiDAR odometry, have a combined processing time of 18.3 ms. The back-end mapping module is 37.2 ms. Both timings are shorter than the data acquisition interval required by the LiDAR's sampling frequency (10 Hz) and the map generation frequency (2 Hz), respectively, confirming the real-time performance of our LOAM module.

For the conversion module, the computational time required to transform the voxel map into the 2D structural semantic map depicted in Figure 13. The voxel map update time scales with map size, and this time cost is particularly pronounced in open environments compared to enclosed scenes [41]. In our experiments, Area A is the only trajectory that includes loop closures, resulting in significantly lower computation times compared to areas B and C, which are focused on open area exploration. This difference arises because in loop-back scenarios, only the updated map segments require modification, while open-area exploration triggers broader map updates. Despite this, the median map conversion time for areas B and C is approximately 1s, with a maximum of 2.8s. These update times are sufficient within the requirements for real-time decision making and control on a USV driving at up to 3m/s, given a 150m LiDAR sensing range.

The IENC integration module, primarily designed for long-term maintenance and sharing of known environment maps, is executed offline. This approach ensures that the generated IENC-compatible data maintain high accuracy and stability without imposing additional computational cost during navigation tasks.

V. CONCLUSION

In this paper, we propose Inland-LOAM, an integrated LiDAR-only SLAM framework specifically designed for robust odometry, mapping, and structural semantic map generation in challenging inland waterway environments. Addressing

²<https://www.openstreetmap.org>

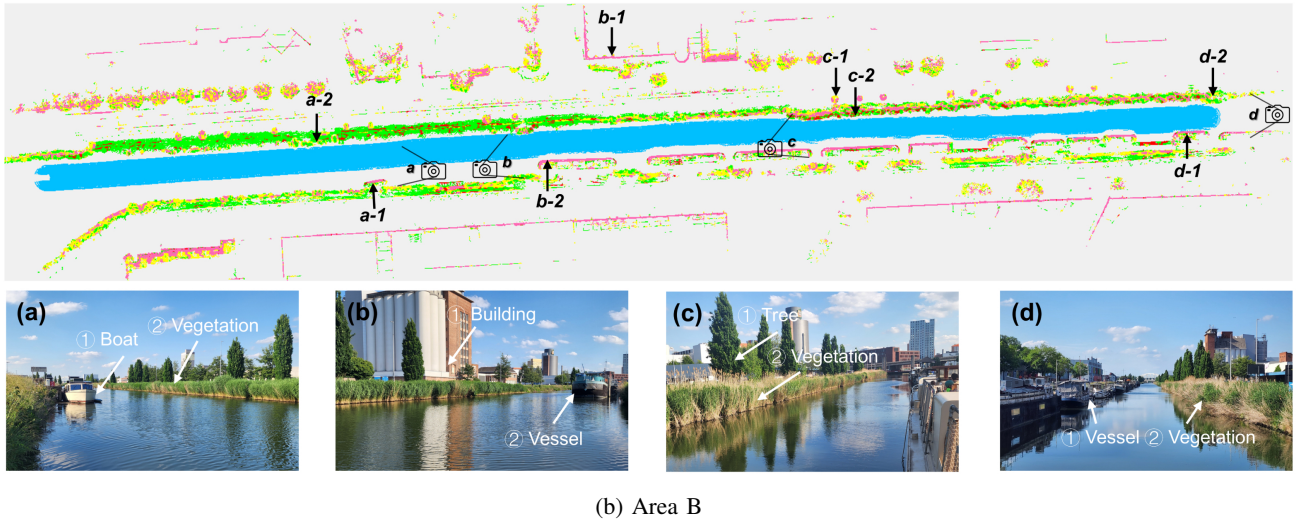
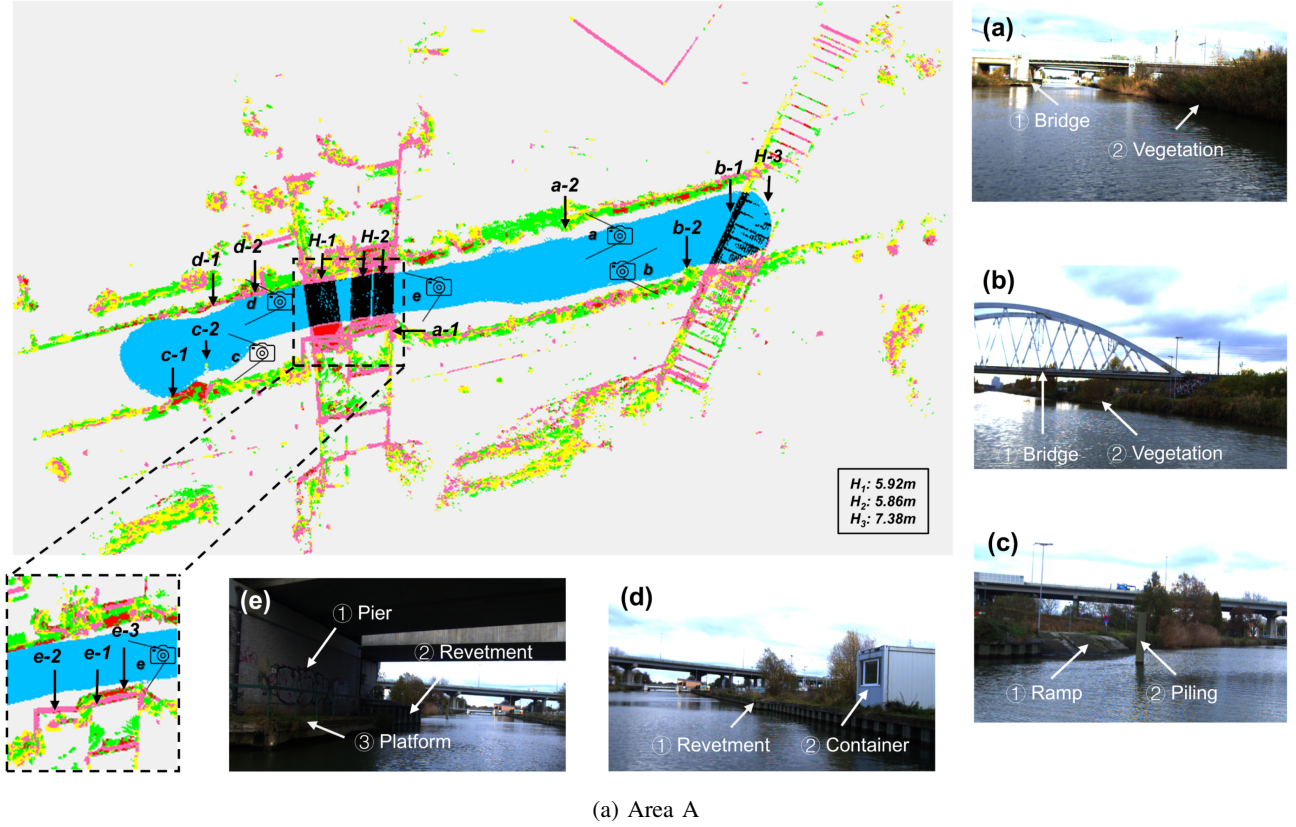


TABLE III: Processing Time for the Components of LOAM Module.

Component	Time (ms)
Pre-processing & Plane Fitting	7.8
Feature Extraction & LiDAR Odometry	10.5
Mapping	37.2

the limitations of conventional SLAM methods, our contributions include an enhanced feature extraction approach and a joint optimization method that uses the water surface as a globally consistent planar reference to effectively reduce

drift. Furthermore, we detailed an end-to-end pipeline transforming dense 3D point clouds into structured, semantic 2D maps. The proposed voxel-based semantic segmentation and subsequent 2D mapping method allow real-time estimation of critical navigational parameters, such as bridge clearances, and provide precisely delineated shorelines compatible with IENC standards.

Through comprehensive experiments conducted on our collected dataset, Inland-LOAM demonstrated superior performance in terms of localization precision and semantic map quality compared to the state-of-the-art methods. Semantic maps provide detailed, up-to-date, and actionable insights,

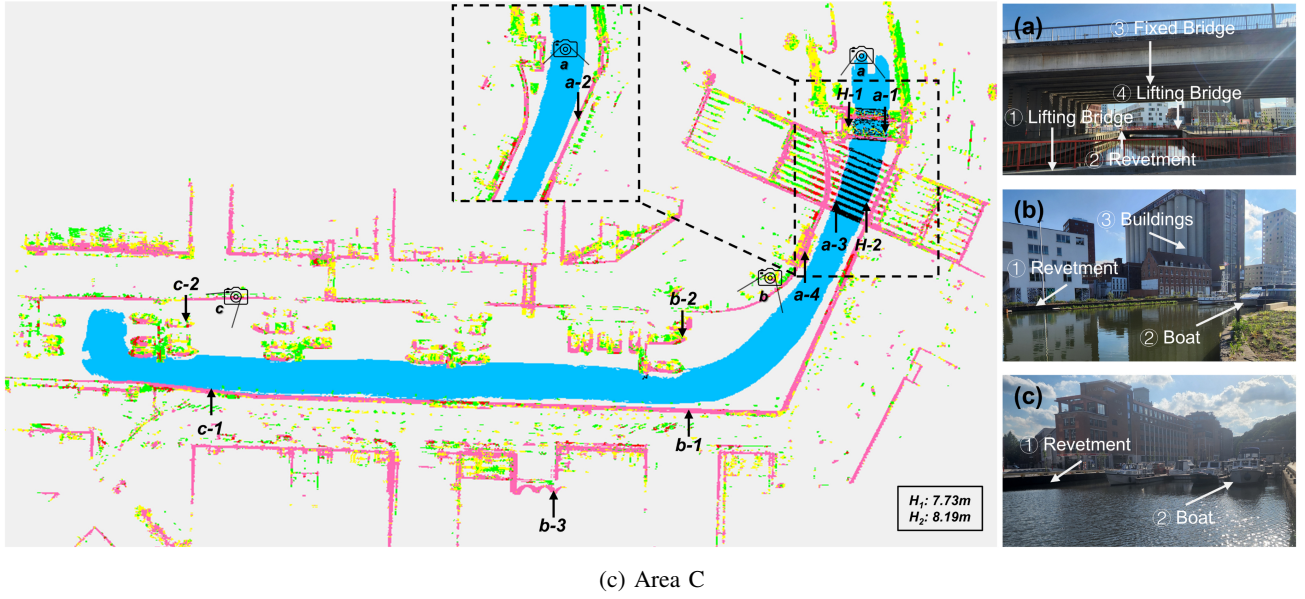


Fig. 11: Structural semantic maps generated by Inland-LOAM in areas A, B, and C. Each scenario is presented with corresponding real-world photographs from multiple perspectives, annotated to explain key features. The color encoding corresponds to the semantic classes defined in Section III-D2: red for Horizontal Planar Surfaces (HP), pink for Vertical Planar Surfaces (VP), green for Complex Horizontal Terrain (CH), yellow for Complex Vertical Structures (CV), blue for Open Water Surface (OW), and black for Under Bridge Clearance Zone (UB). Note that this color scheme is used for visualization purposes only and does not represent the traditional cost definitions in a costmap. For (a) and (c), detailed semantic maps of bridge areas are included, with the identified clearance height explicitly labeled (H).

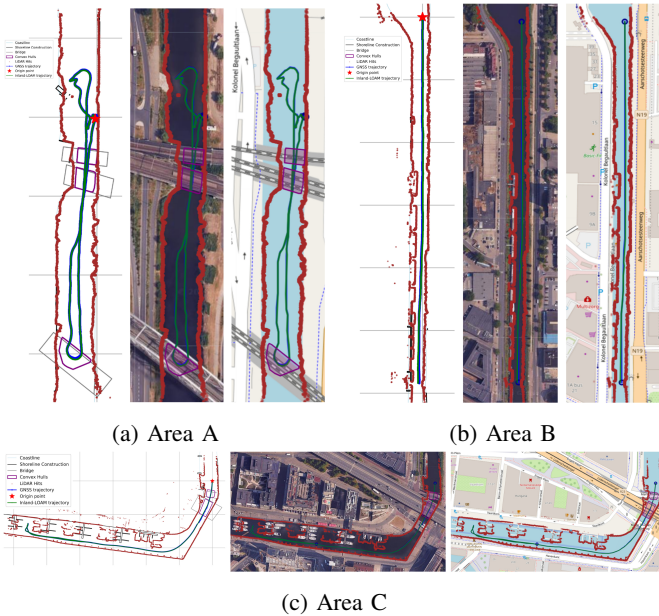


Fig. 12: The shoreline boundaries generated by Inland-LOAM were projected onto the IENC, Google Earth, and OpenStreetMap datasets in areas A, B, and C, respectively.

enhancing navigational safety and operational efficiency for autonomous vessels.

However, our method has certain limitations. Purely geometric-based classification exhibits ambiguity in regions with complex natural textures, such as densely vegetated areas,

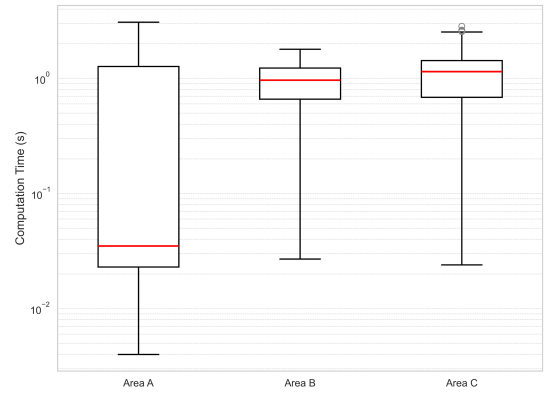


Fig. 13: The computation time to update the 2D map generated from the voxel map under different exploration areas.

leading to occasional misclassification at a local scale. Additionally, the current static mapping approach faces challenges when encountering dynamic elements, as evidenced by the aliasing artifacts caused by moving lifting bridges. Reliable detection of the water surface itself can also be compromised in highly dynamic circumstances, such as in the presence of nearby moving vessels, which can degrade the effectiveness of our global planar constraint and introduce additional drift. This highlights potential vulnerabilities when operating in environments with significant dynamic infrastructure or dense vessel traffic.

Future research will focus on addressing these limitations. One promising direction is to enhance semantic classifica-

tion accuracy by integrating additional sensor modalities, particularly RGB cameras. Leveraging color and texture information could help resolve semantic ambiguities among geometrically similar but semantically distinct surfaces. To improve robustness in dynamic environments, the framework could be extended with temporal analysis and multi-object tracking capabilities. Moreover, the generated semantic maps pave the way for higher-level autonomous applications, such as semantic-guided localization using stable landmarks like building facades or revetments, and path planning based on semantic costmaps.

ACKNOWLEDGMENT

The authors would like to thank the Editor-in-Chief, an Associate Editor, and anonymous referees for their invaluable comments and suggestions.

REFERENCES

- [1] European Commission. (2024) Inland waterways. [Online]. Available: https://transport.ec.europa.eu/transport-modes/inland-waterways_en
- [2] —, “Proposal for a DIRECTIVE of the European Parliament and of the Council amending Directive 2005/44/EC on harmonised river information services (RIS) on inland waterways in the Community,” European Commission, Tech. Rep. COM(2024) 33 final, January 2024. [Online]. Available: <https://eur-lex.europa.eu/legal-content/EN/TXT/?uri=CELEX%3A52024PC0033>
- [3] A. Galieriková, “The human factor and maritime safety,” *Transportation Research Procedia*, vol. 40, pp. 1319–1326, 2019, tRANSCOM 2019 13th International Scientific Conference on Sustainable, Modern and Safe Transport.
- [4] W. Wang, B. Gheneti, L. A. Mateos, F. Duarte, C. Ratti, and D. Rus, “Roboat: An autonomous surface vehicle for urban waterways,” in *2019 IEEE/RSJ International Conference on Intelligent Robots and Systems (IROS)*, 2019, pp. 6340–6347.
- [5] P. Segovia, V. Puig, R. R. Negenborn, and V. Reppa, “Dynamic coordination of multiple movable bridges and vessels for time-efficient inland waterway navigation,” *IEEE Transactions on Intelligent Transportation Systems*, 2025.
- [6] N. Kamal, “Inland electronic navigation charts for enhancing the efficiency of navigational waterway in the Nile river case study-el-wasta reach,” *International Water Technology Journal*, vol. 7, no. 4, 2017.
- [7] W. Wang, T. Shan, P. Leoni, D. Fernández-Gutiérrez, D. Meyers, C. Ratti, and D. Rus, “Roboat ii: A novel autonomous surface vessel for urban environments,” in *2020 IEEE/RSJ International Conference on Intelligent Robots and Systems (IROS)*. IEEE, 2020, pp. 1740–1747.
- [8] T. Kriechbaumer, K. Blackburn, T. P. Breckon, O. Hamilton, and M. Rivas Casado, “Quantitative evaluation of stereo visual odometry for autonomous vessel localisation in inland waterway sensing applications,” *Sensors*, vol. 15, no. 12, pp. 31 869–31 887, 2015.
- [9] J. Fuentes-Pacheco, J. Ruiz-Ascencio, and J. M. Rendón-Mancha, “Visual simultaneous localization and mapping: a survey,” *Artificial intelligence review*, vol. 43, pp. 55–81, 2015.
- [10] S. Van Baelen, H. Shin, G. Peeters, M. R. Afzal, G. Yayla, and P. Slaets, “Preliminary results on increased situational awareness for inland vessels using onboard lidar,” in *Global Oceans 2020: Singapore – U.S. Gulf Coast*, 2020, pp. 1–6.
- [11] F. Pieper and A. Hahn, “A conceptual approach to harbor object detection: The potential of 3d-lidar-based sensor fusion for high precision enc,” *IFAC-PapersOnLine*, vol. 58, no. 20, pp. 415–420, 2024.
- [12] L. Hösch, A. Llorente, A. An, J. P. Llerena, and D. Medina, “High definition mapping for inland waterways: Techniques, challenges and prospects,” in *2023 IEEE 26th International Conference on Intelligent Transportation Systems (ITSC)*. IEEE, 2023, pp. 6034–6041.
- [13] M. Zhao, X. Guo, L. Song, B. Qin, X. Shi, G. H. Lee, and G. Sun, “A general framework for lifelong localization and mapping in changing environment,” in *2021 IEEE/RSJ International Conference on Intelligent Robots and Systems (IROS)*. IEEE, 2021, pp. 3305–3312.
- [14] G. He, X. Yuan, Y. Zhuang, and H. Hu, “An integrated gnss/lidar-slam pose estimation framework for large-scale map building in partially gnss-denied environments,” *IEEE Transactions on Instrumentation and Measurement*, vol. 70, pp. 1–9, 2021.
- [15] J. Zhang, S. Singh *et al.*, “Loam: Lidar odometry and mapping in real-time,” in *Robotics: Science and systems*, vol. 2, no. 9. Berkeley, CA, 2014, pp. 1–9.
- [16] T. Shan and B. Englot, “Lego-loam: Lightweight and ground-optimized lidar odometry and mapping on variable terrain,” in *2018 IEEE/RSJ International Conference on Intelligent Robots and Systems (IROS)*. IEEE, 2018, pp. 4758–4765.
- [17] E. Wouters. (2023, 4) IN BEELD. Na de zelfrijdende wagen, de zelfvarende boot: “Kijk, zonder handen!”. Het Laatste Nieuws. [Online]. Available: <https://www.hln.be/leuven/in-beeld-na-de-zelfrijdende-wagen-de-zelfvarende-boot-kijkzonder-handen~a6c2ac48/>
- [18] Z. Luo, S. van Baelen, P. Slaets, and H. Bruyninckx, “Enhancing inland waterway transport through lidar-based updates to electronic navigational charts,” in *OCEANS 2024-Halifax*. IEEE, 2024, pp. 01–08.
- [19] D. Thompson, E. Coyle, and J. Brown, “Efficient lidar-based object segmentation and mapping for maritime environments,” *IEEE Journal of Oceanic Engineering*, vol. 44, no. 2, pp. 352–362, 2019.
- [20] K. Dietmayer, J. Schwenninger, H. Gupta, M. Saad, M. Lipka, M. Overbeck, and W. Felber, “Smart port shuttle: Sensor-based navigation for inland waterway transportation,” *Engineering Proceedings*, vol. 54, no. 1, p. 50, 2023.
- [21] N. Wang, H. Zhao, and T. Chen, “Dr-liom: Direct registration lidar-inertial odometry and mapping for uncrewed surface vehicles in a harbor,” *IEEE Transactions on Intelligent Transportation Systems*, 2025.
- [22] H. Bavle, J. L. Sanchez-Lopez, M. Shaheer, J. Civera, and H. Voos, “Situational graphs for robot navigation in structured indoor environments,” *IEEE Robotics and Automation Letters*, vol. 7, no. 4, pp. 9107–9114, 2022.
- [23] Q. Zou, Q. Sun, L. Chen, B. Nie, and Q. Li, “A comparative analysis of lidar slam-based indoor navigation for autonomous vehicles,” *IEEE Transactions on Intelligent Transportation Systems*, vol. 23, no. 7, pp. 6907–6921, 2021.
- [24] Z. Chen, Y. Qi, D. Feng, X. Zhuang, H. Chen, X. Hu, J. Wu, K. Peng, and P. Lu, “Heterogeneous lidar dataset for benchmarking robust localization in diverse degenerate scenarios,” 2024. [Online]. Available: <https://arxiv.org/abs/2409.04961>
- [25] I. Filip, C. Lass, and D. Medina, “Performance evaluation of visual and lidar slam for inland waterways,” in *2024 24th International Conference on Control, Automation and Systems (ICCAS)*, 2024, pp. 562–567.
- [26] —, “Performance evaluation of visual and lidar slam for inland waterways,” in *2024 24th International Conference on Control, Automation and Systems (ICCAS)*. IEEE, 2024, pp. 562–567.
- [27] Y. Cheng, M. Jiang, J. Zhu, and Y. Liu, “Are we ready for unmanned surface vehicles in inland waterways? the usinland multisensor dataset and benchmark,” *IEEE Robotics and Automation Letters*, vol. 6, no. 2, pp. 3964–3970, 2021.
- [28] A. Geiger, P. Lenz, and R. Urtasun, “Are we ready for autonomous driving? the kitti vision benchmark suite,” in *2012 IEEE conference on computer vision and pattern recognition*. IEEE, 2012, pp. 3354–3361.
- [29] H. Wang, C. Wang, C.-L. Chen, and L. Xie, “F-loam: Fast lidar odometry and mapping,” in *2021 IEEE/RSJ International Conference on Intelligent Robots and Systems (IROS)*. IEEE, 2021, pp. 4390–4396.
- [30] K. Koide, J. Miura, and E. Menegatti, “A portable three-dimensional lidar-based system for long-term and wide-area people behavior measurement,” *International Journal of Advanced Robotic Systems*, vol. 16, no. 2, p. 1729881419841532, 2019.
- [31] X. Wei, J. Lv, J. Sun, and S. Pu, “Ground-slam: Ground constrained lidar slam for structured multi-floor environments,” *arXiv preprint arXiv:2103.03713*, 2021.
- [32] I. Vizzo, T. Guadagnino, B. Mersch, L. Wiesmann, J. Behley, and C. Stachniss, “Kiss-icp: In defense of point-to-point icp—simple, accurate, and robust registration if done the right way,” *IEEE Robotics and Automation Letters*, vol. 8, no. 2, pp. 1029–1036, 2023.
- [33] X. Chen, A. Milioto, E. Palazzolo, P. Giguere, J. Behley, and C. Stachniss, “Suma++: Efficient lidar-based semantic slam,” in *2019 IEEE/RSJ International Conference on Intelligent Robots and Systems (IROS)*. IEEE, 2019, pp. 4530–4537.
- [34] A. Milioto, I. Vizzo, J. Behley, and C. Stachniss, “Rangenet++: Fast and accurate lidar semantic segmentation,” in *2019 IEEE/RSJ international conference on intelligent robots and systems (IROS)*. IEEE, 2019, pp. 4213–4220.
- [35] Z. Gong, J. Li, Z. Luo, C. Wen, C. Wang, and J. Zelek, “Mapping and semantic modeling of underground parking lots using a backpack lidar system,” *IEEE Transactions on Intelligent Transportation Systems*, vol. 22, no. 2, pp. 734–746, 2019.
- [36] K. Wei, X. Li, Z. Tian, P. Ni, and Z. Sun, “A semantic-aided fusion localization method for intelligent vehicles in gnss-denied dynamic

- environments,” *IEEE Transactions on Intelligent Vehicles*, pp. 1–12, 2024.
- [37] A. Vaswani, N. Shazeer, N. Parmar, J. Uszkoreit, L. Jones, A. N. Gomez, Ł. Kaiser, and I. Polosukhin, “Attention is all you need,” *Advances in neural information processing systems*, vol. 30, 2017.
 - [38] L. Zhou, G. Huang, Y. Mao, J. Yu, S. Wang, and M. Kaess, “*PCC-lislam*: Lidar slam with planes, lines, and cylinders,” *IEEE Robotics and Automation Letters*, vol. 7, no. 3, pp. 7163–7170, 2022.
 - [39] L. C. de Lima, M. Ramezani, P. Borges, and M. Brünig, “Air-ground collaborative localisation in forests using lidar canopy maps,” *IEEE Robotics and Automation Letters*, vol. 8, no. 3, pp. 1818–1825, 2023.
 - [40] R. Pfliegl and A. Bäck, “Increasing the attractiveness of inland waterway transport with e-transport river information services,” *Transportation research record*, vol. 1963, no. 1, pp. 15–22, 2006.
 - [41] S. Fredriksson, A. Saradagi, and G. Nikolakopoulos, “Voxel map to occupancy map conversion using free space projection for efficient map representation for aerial and ground robots,” *IEEE Robotics and Automation Letters*, 2024.
 - [42] M. Kaess, H. Johannsson, R. Roberts, V. Ila, J. J. Leonard, and F. Dellaert, “*isam2*: Incremental smoothing and mapping using the bayes tree,” *The International Journal of Robotics Research*, vol. 31, no. 2, pp. 216–235, 2012.
 - [43] F. Dellaert and G. Contributors, “*borglab/gtsam*,” May 2022. [Online]. Available: <https://github.com/borglab/gtsam>
 - [44] A. Elfes, “Using occupancy grids for mobile robot perception and navigation,” *Computer*, vol. 22, no. 6, pp. 46–57, 1989.
 - [45] M. J. Allis, W. L. Peirson, and M. L. Banner, “Application of lidar as a measurement tool for waves,” in *ISOPE International Ocean and Polar Engineering Conference*. ISOPE, 2011, pp. ISOPE-I.
 - [46] R. Buchanan, “Allan variance ros,” Nov. 2021. [Online]. Available: https://github.com/ori-drs/allan_variance_ros
 - [47] T. Kim, G. Pak, and E. Kim, “Gril-calib: Targetless ground robot imu-lidar extrinsic calibration method using ground plane motion constraints,” *IEEE Robotics and Automation Letters*, vol. 9, no. 6, pp. 5409–5416, 2024.
 - [48] D. Griesser, G. Umlauf, and M. O. Franz, “Visual pitch and roll estimation for inland water vessels,” in *2023 IEEE International Conference on Robotics and Automation (ICRA)*. IEEE, 2023, pp. 1961–1967.
 - [49] M. Himmelsbach, F. V. Hundelshausen, and H.-J. Wuensche, “Fast segmentation of 3d point clouds for ground vehicles,” in *2010 IEEE Intelligent Vehicles Symposium*. IEEE, 2010, pp. 560–565.
 - [50] M. A. Fischler and R. C. Bolles, “Random sample consensus: a paradigm for model fitting with applications to image analysis and automated cartography,” *Communications of the ACM*, vol. 24, no. 6, pp. 381–395, 1981.
 - [51] I. Bogoslavskyi and C. Stachniss, “Fast range image-based segmentation of sparse 3d laser scans for online operation,” in *2016 IEEE/RSJ International Conference on Intelligent Robots and Systems (IROS)*. IEEE, 2016, pp. 163–169.
 - [52] P. J. Besl and N. D. McKay, “Method for registration of 3-d shapes,” in *Sensor fusion IV: control paradigms and data structures*, vol. 1611. Spie, 1992, pp. 586–606.
 - [53] M. Ester, H.-P. Kriegel, J. Sander, X. Xu *et al.*, “A density-based algorithm for discovering clusters in large spatial databases with noise,” in *kdd*, vol. 96, no. 34, 1996, pp. 226–231.